A Framework for Optimization on Battery Cycle Life

Xianke Lin [a] **and Wei Lu** [z]

Department of Mechanical Engineering, University of Michigan, Ann Arbor, Michigan 48109, USA

In this study we develop a general approach to optimize battery cycle life while fulfilling both energy and power requirements. By investigating the impact of various battery parameters on energy density, power density and battery cycle life, we find that traditional energy and power density optimization does not lead to good battery cycle life: they have to be optimized together. This paper provides the battery cycle life optimization framework, algorithm and procedure that integrate energy density and power density constraints. We find that higher energy and power densities require smaller particle sizes in both the anode and the cathode, while better battery cycle life requires larger particle size in the anode and smaller particle size in the cathode. A significant increase of cycle life can be achieved by targeting an energy density slightly lower than the achievable maximum to free up the design space. The optimization procedure developed in this study can provide useful guidance for battery design and manufacturing.
 [DOI: 10.1149/2.0741814jes]

Manuscript submitted July 27, 2018; revised manuscript received October 1, 2018. Published October 30, 2018.

Battery longevity is crucial in transportation electrification.[1] While a battery life of 3–5 years is acceptable for consumer electronics, such a short service time would be a major drawback for electric vehicles.[2,3] Battery pack replacement incurs an expense comparable to the replacement of an engine or transmission. In addition, simply increasing the duration of each charge by minimizing the energy consumption of a battery-powered system will not necessarily maximize the lifetime of the battery pack.[4] While several studies have been done to optimize battery performance, the focus was on the optimization of energy and power densities. Fuller et al.[5] investigated the dual lithium ion insertion cell and optimized its energy and power densities by using the Newman's battery model. Sumitava et al.[6] developed a model-based procedure to optimize battery parameters, including electrode porosities and thickness, to maximize the energy draw for a given set of applied current, cutoff voltage, and total amount of discharge time. Advanced control algorithms were also developed to help improve the lifetime of a battery. Moura et al.[7,8] developed a battery management strategy based on a solid electrolyte interphase (SEI) growth model to protect battery health during charging and discharging. This control algorithm can optimize the power management for specific batteries and application configurations to maximize the battery performance. However, it does not optimize the battery design. These efforts highlight the significance and great potential of battery optimization. So far a direct relationship between battery cycle life and optimal battery parameters has not yet been established. In this study we develop a general approach to optimize battery cycle life while fulfilling both energy and power requirements.

A substantial amount of experimental, theoretical and computational studies have been performed in an attempt to characterize and understand battery capacity degradation. Ramadass et al.[9] identified that the key factors of capacity degradation were losses of rate capability, primary active material and secondary active material after systematic degradation analysis of cycled 18650 cells. Safari et al.[10] modeled capacity degradation in terms of SEI growth on the anode and the associated lithium ion consumption. Calibrating a single particle model using experimental cycling data, Zhang et al.[11] suggested that capacity degradation may involve multiple stages. Recently a comprehensive physics-based degradation model was developed by integrating the key degradation mechanisms: SEI growth and manganese deposition on the anode electrode, manganese dissolution, electrolyte oxidation, and salt decomposition on the cathode electrode.[12] In this study we further extend the side-reaction coupled degradation model by incorporating the effect of mechanics and mechanical degradation, and then use it to demonstrate the framework, algorithm and procedure for battery cycle life optimization. We find that battery cycle life can be improved by reducing the capacity degradation through parameter optimization, while maintaining high target energy and power densities, even when the battery material system is fixed. The optimization approach developed in this study would be useful for battery design and manufacturing as well as the battery management strategy.

Degradation Model

We consider a full cell consisting of a graphite anode, a separator, and a lithium manganese oxide (LMO) cathode in the $LiPF_6$ ethylene carbonate (EC)/dimethyl carbonate (DMC) electrolyte. Here we select the LMO/graphite system since LMO is a low-cost, environmentally friendly, and highly abundant material for the Li-ion battery cathode, and many of its material parameters are readily available. We first extend a previously validated degradation model[12] by adding the effect of mechanical stress, and then use this extended degradation model for optimization. The degradation model consists of two levels: the particle level and the cell level. The modeling at the particle level describes lithium intercalation/deintercalation, diffusion in the particle, and side reactions at the interface between the solid particle and the electrolyte. The electrochemical model at the cell level, which is based on the porous electrode theory,[5,13,14] describes the transport of lithium ions and other species including Mn^{2+}, H^+, and H_2O. The two levels are coupled through the local reaction current. Fig. 1 summarizes the side reactions in the degradation model[12] and their interactions. The side reactions on the anode surface include SEI growth and manganese deposition, which are mainly responsible for the loss of cyclable lithium ions. The side reactions on the cathode side, including manganese dissolution, electrolyte oxidation, and salt decomposition, mainly lead to the loss of active material and capacity degradation of the cathode.

Now we extend the degradation model to add the effect of mechanical stress. The lattice constant changes as Li intercalates into or deintercalates out of the $LiMn_2O_4$ particle,[15] and it may be assumed to change linearly with Li stoichiometry.[16,17] Stress is generated when the lattice change is not uniform in the particle as a result of concentration gradient. Stress-induced particle fracture is one of the major degradation mechanisms in the cathode.[18] Similar as previous works,[18] here we assume the active material particle is spherical and the material is linearly elastic. Linear elastic analysis and small deformation theory are applicable for materials such as $LiMn_2O_4$ because the intercalation-induced deformation is small and less than a few percent. With spherical symmetry, the stress, strain and displacement fields are functions of only the radial coordinate of the particle.

The equilibrium equation in a spherical particle of the cathode is given by[18]

$$\frac{d\sigma_r}{dr} + \frac{2}{r}(\sigma_r - \sigma_t) = 0 \qquad [1]$$

[a]Present address: Department of Automotive, Mechanical and Manufacturing Engineering, University of Ontario Institute of Technology, Oshawa, Ontario L1H 7K4, Canada.
[z]E-mail: weilu@umich.edu

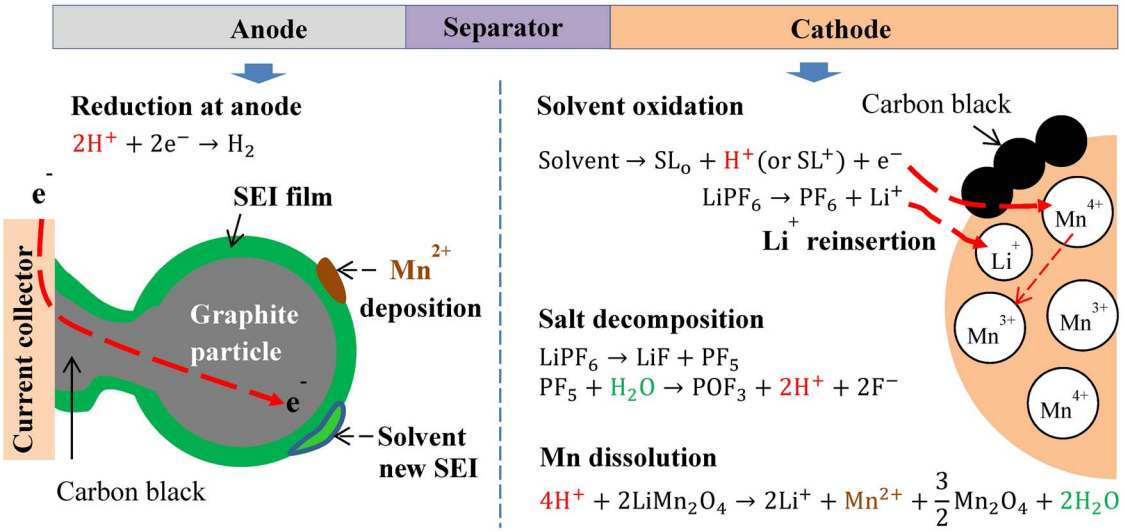

Figure 1. A schematic diagram of side reactions in the degradation model.

where σ_r is the radial stress, σ_t is the tangential stress, and r is the radial coordinate of the particle.

With consideration of intercalation strain, the stress-strain relation in the particle is given by[18]

$$\varepsilon_r = \frac{1}{E}(\sigma_r - 2\upsilon\sigma_t) + \frac{\Omega}{3}\tilde{c}_1 \quad [2]$$

$$\varepsilon_t = \frac{1}{E}[\sigma_t - \upsilon(\sigma_r + \sigma_t)] + \frac{\Omega}{3}\tilde{c}_1 \quad [3]$$

where ε_r is the radial strain, ε_t is the tangential strain, E is Young's modulus of the active particle, υ is the Poisson's ratio, Ω is the partial molar volume of lithium ion in the particle, and $\tilde{c}_1 = c_1 - c_{10}$ is the difference between lithium concentration in the particle at the current state, c_1, and at the initial stress-free state, c_{10}.

The equation for the strain-displacement relation is

$$\varepsilon_r = \frac{du}{dr}\ , \varepsilon_t = \frac{u}{r} \quad [4]$$

where u is the radial displacement. Using the displacement, the equilibrium equation can be rewritten as[18]

$$\frac{d}{dr}\left(\frac{1}{r^2}\frac{d}{dr}\left(r^2u\right)\right) = \frac{1+\upsilon}{1-\upsilon}\frac{\Omega}{3}\frac{d\tilde{c}_1}{dr} \quad [5]$$

The displacement can be obtained by integrating Eq. 5 twice. Two integration constants will appear during the integration, and they can be determined by the boundary conditions of $u(0) = 0$ and $\sigma_r(r_p) = 0$, where r_p is the particle radius.

The stress are then given by[18]

$$\sigma_r(r) = \frac{2\Omega E}{3(1-\upsilon)}\left(\frac{1}{r_p^3}\int_0^{r_p}\tilde{c}_1 r^2 dr - \frac{1}{r^3}\int_0^{r}\tilde{c}_1 r^2 dr\right) \quad [6]$$

$$\sigma_t(r) = \frac{\Omega E}{3(1-\upsilon)}\left(\frac{2}{r_p^3}\int_0^{r_p}\tilde{c}_1 r^2 dr + \frac{1}{r^3}\int_0^{r}\tilde{c}_1 r^2 dr - \tilde{c}_1\right) \quad [7]$$

The electrochemical potential in an ideal solid solution can be expressed as[19]

$$\mu = \mu_0 + RT\ln X - \Omega\sigma_h \quad [8]$$

where μ_0 is the electrochemical potential at a reference state, R is the gas constant, T is temperature, X is the mole fraction, and σ_h is the hydrostatic stress given by

$$\sigma_h = \frac{\sigma_r + 2\sigma_t}{3} = \frac{2\Omega E}{9(1-\upsilon)}\left(\frac{3}{r_p^3}\int_0^{r_p}\tilde{c}_1 r^2 dr - \tilde{c}_1\right) \quad [9]$$

Note that the tangential stress on the particle surface is given by $\sigma_t(r_p) = (3/2)\sigma_h(r_p)$, which scales with the hydrostatic stress on the particle surface. The hydrostatic stress or the tangential stress on the particle surface leads to loss of materials and reduction of usable volume fraction. To account for this effect, we use the damage mechanics concept and update the usable volume fraction, $\varepsilon_{usable}^{pos}$, so that its rate of change is related to the hydrostatic stress on the particle surface by $d\varepsilon_{usable}^{pos}(x,t)/dt = f(\sigma_h(x,r_p))$, where x is the coordinate along the thickness direction of the electrode and f is a damage function.[20] The damage function and parameters can be determined by fitting experimental measurements. The active surface area per unit electrode volume in the cathode, a_s, is given by $a_s = 3\varepsilon_{usable}^{pos}/r_p$. Therefore, a reduction of $\varepsilon_{usable}^{pos}$ leads to a smaller active surface area.

The lithium diffusion flux along the radial direction, J, is related to the gradient of the chemical potential by

$$J = -Mc_1\frac{\partial\mu}{\partial r} \quad [10]$$

where M is the mobility. With $\partial(\ln X)/\partial r = (1/c_1)\partial c_1/\partial r$ and $D = MRT$, we can write

$$J = -D\left(\frac{\partial c_1}{\partial r} - \frac{\Omega c_1}{RT}\frac{\partial\sigma_h}{\partial r}\right) \quad [11]$$

where D is the diffusion coefficient.

Mass conservation requires the time rate of concertation change equals to the negative of the divergence of the diffusional flux, or $\partial c_1/\partial t = -\partial(r^2J)/(r^2\partial r)$. This gives a diffusion equation in the form of

$$\frac{\partial c_1}{\partial t} = D\left[\frac{\partial^2 c_1}{\partial r^2} + \frac{2}{r}\frac{\partial c_1}{\partial r} + b\left(\frac{\partial c_1}{\partial r}\right)^2 + bc_1\left(\frac{\partial^2 c_1}{\partial r^2} + \frac{2}{r}\frac{\partial c_1}{\partial r}\right)\right] \quad [12]$$

where $b = 2\Omega^2 E/[9(1-\upsilon)RT]$. The first two terms on the right side of Eq. 12 are the regular terms for diffusion driven by the concentration gradient. The last two terms account for the additional effect from intercalation stress.

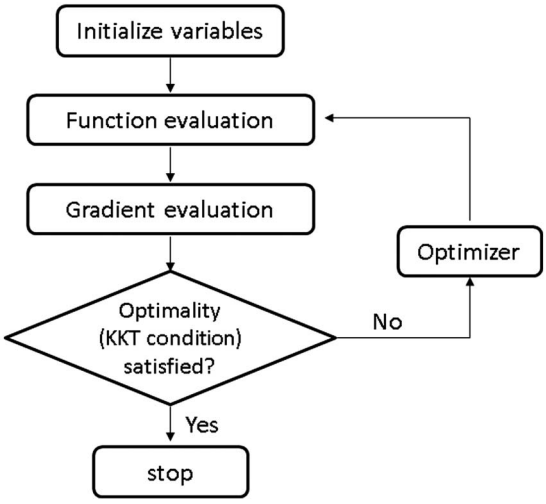

Figure 2. Flowchart of the gradient based optimization scheme.

The flux boundary condition is given on the particle surface by

$$r = r_p : -D\,(1 + bc_1)\,\frac{\partial c_1}{\partial r}\bigg|_{r=r_p} = \frac{i_{Li}}{F} \qquad [13]$$

where i_{Li} is the lithium intercalation/deintercalation current with the deintercalation current defined positive.

Gradient-Based Optimization

Studies have shown that battery design parameters can have a significant impact on energy density and power density.[6,14,21–24] In this study we investigate the optimization of several main design parameters to maximize the cycle life, while at the same time meeting the power density and energy density requirements. The initial parameter values are determined by optimizing the energy density first with the required power density as a constraint. Then the battery cycle life will be optimized by minimizing the battery degradation over long-term cycling with the required power density and energy density as constraints. We focus on controllable cell fabrication parameters, including particle size, thickness, porosity, and cathode conductivity, while all other material parameters are known and kept fixed.

Optimization framework.—A general optimization problem has the following form:

$$\text{minimize } f\,(x)\,, \quad f : \mathrm{R}^n \to \mathrm{R} \qquad [14]$$

$$\text{subject to } \begin{cases} x_{lower} \le x \le x_{upper} \\ g_i\,(x) \le 0, \quad i = 1, \ldots, m \\ h_i\,(x) = 0, \quad i = 1, \ldots, p \end{cases} \qquad [15]$$

where $f(x)$ is the objective function to be minimized over the variable x, $g_i(x)$ are called inequality constraints, and $h_i(x)$ are called equality constraints. In this study, the objective function for minimization is the battery capacity degradation after prolonged cycling. While minimization is used as an example here, maximization can be treated similarly by flipping the sign of the objective function.

Different optimization algorithms, including genetic algorithms and gradient descent algorithms, have been used in other aspects of battery research.[25,26] In this study, the calculation of the gradient is straightforward, therefore we employ the gradient-descent scheme.[27] The process of gradient calculation and variable optimization is shown in Fig. 2.

The first-order condition necessary for a solution to be minimal in nonlinear programming is the Karush-Kuhn-Tucker (KKT) condition,[28] which can be expressed by

$$\nabla f(x^*) + \sum_{i=1}^{m} \mu_i \nabla g_i(x^*) + \sum_{i=1}^{p} \lambda_i \nabla h_i(x^*) = 0 \qquad [16]$$

$$\mu_i \ge 0, \text{ for all } i = 1, \ldots, m \qquad [17]$$

$$\mu_i g_i(x^*) = 0, \text{ for all, } i = 1, \ldots, m \qquad [18]$$

where x^* is an optimal solution, μ_i and λ_i are the Lagrange multipliers associated with the inequality and equality constraints, respectively.

Optimization method.—In this study, sequential quadratic programming (SQP) is used as the gradient-based optimization method. SQP solves a sequence of optimization sub-problems, each of which optimizes a quadratic model of the objective subject to a linearization of the constraints. The sub-problem at each iteration x_k can be expressed by[29]

$$\text{minimize } \frac{1}{2} d^T H_k d + \nabla f(x_k)^T d \qquad [19]$$

$$\nabla g_i(x_k)^T d + g_i\,(x_k) \le 0, \text{ for all } i = 1, \ldots, m \qquad [20]$$

$$\nabla h_i(x_k)^T d + h_i\,(x_k) = 0, \text{ for all } i = 1, \ldots, p \qquad [21]$$

where $d = x - x_k$ and the matrix H_k is a positive definite approximation of the Hessian matrix of the Lagrangian function. This sub-problem can be solved using the quadratic programming algorithm. The solution is used to form a new iterate at

$$x_{k+1} = x_k + \alpha_k d_k \qquad [22]$$

where α_k is a step length parameter. The step length parameter is determined by a line search algorithm to produce a sufficient decrease in a merit function.[30,31] The goal is to calculate a sufficiently accurate step length parameter in as few function evaluations as possible so that the underlying algorithm converges.[32]

In this work we use the finite element software COMSOL for degradation modeling and use Matlab for optimization. COMSOL has a predefined battery model but it is not sufficient for the complex side reaction-coupled battery model in this study and lacks the flexibility to add new equations or change existing equations. Therefore, the degradation model is developed in COMSOL by direct implementation of all the fundamental relations in Ref. 12 and in this work. With the Matlab Livelink interface in COMSOL, we use a Matlab script to run COMSOL models in a COMSOL server and pass simulation results to Matlab at each step for optimization.

Problem setup.—The power density requirement is chosen first and fixed as a constraint. The energy density is then maximized by using the numerical optimization framework described in the previous section. Matlab optimization toolbox is used in this study. The battery parameters obtained after maximizing the energy density while fulfilling the power density constraint are used as the starting point for battery cycle life optimization. In the battery cycle life optimization, the power density requirement is still fixed, while the energy density requirement is prescribed to be slightly less than the maximum from the energy density optimization to give the optimization algorithm some freedom to search for parameters that minimize capacity degradation.

In the first step, the cell is charged at 0.1 C to 4.15 V. Next, the cell is cycled for 10 formation cycles in the simulation at 0.1 C charge and discharge rate. Then, the energy density (Wh/kg) is obtained by one galvanostatic discharge cycle of the cell at 1 C rate for 1 hour until reaching a cutoff voltage of 3.5 V. The constant discharge current is adjusted by trying several calculations until the battery is discharged to 3.5 V in exactly 1 hour. In other words, the constant discharge current is determined by a search algorithm rather than being predefined. The power density (W/kg) is obtained by a high discharge rate to a cutoff voltage of 3 V in 10 s.[25] The constant discharge current is adjusted by a search algorithm so that the battery is discharged to 3V in exactly

Table I. Design variables and their bounds.

Design variables	Lower bound	Upper bound
Cathode particle radius (μm)	0.2	20
Cathode thickness (μm)	40	250
Cathode porosity	0.1	0.6
Cathode conductivity (S m^{-1})	1	10
Anode particle radius (μm)	0.2	20
Anode thickness (μm)	40	250
Anode porosity	0.1	0.6

10 s. This cutoff value is selected because further discharge of a battery could lead to irreversible damage. The capacity degradation is represented by the difference in percentage between the discharge capacity at the 100th cycle and the discharge capacity at the 1st cycle.

$$E_{cell} = \frac{1}{M_{cell}} \int_0^{3600} V_{cell}(t) I dt \quad [23]$$

$$P_{cell} = \frac{1}{M_{cell} t_{pulse}} \int_0^{t_{pulse}} V_{cell}(t) I dt \text{ with } t_{pulse} = 10\,\text{s} \quad [24]$$

$$f_{degra} = \frac{C_1 - C_{100}}{C_1} \quad [25]$$

$$M_{cell} = M_{cc-} + M_- + M_{sep} + M_+ + M_{cc+} \quad [26]$$

where E_{cell} is the energy density, P_{cell} is the power density, V_{cell} is the cell terminal voltage, I is the discharge rate, f_{degra} is the relative capacity fade, C_{100} is the discharge capacity at the 100th cycle, C_1 is the discharge capacity at the 1st cycle, M_{cell} is the total cell mass, M_{cc-} is the mass of the negative current collector, M_- is the mass of the negative electrode, M_{sep} is the mass of the separator, M_+ is the mass of the positive electrode, and M_{cc+} is the mass of the positive current collector. The mass of electrodes is a function of electrode thickness and porosity. The energy density optimization is given by

$$\text{maximize } E_{cell} = \frac{1}{M_{cell}} \int_0^{3600} V_{cell}(t) I dt \quad [27]$$

$$\text{subject to } \begin{cases} x_{lower} \le x \le x_{upper} \\ g_1(x) = P_{req} - P_{cell} \le 0 \end{cases} \quad [28]$$

7 design parameters have been selected, which are shown in Table I. Therefore x is a 7-dimensional vector. There are 3 design parameters for the anode: particle size, electrode thickness, and porosity, while there are 4 design parameters for the cathode: particle size, electrode thickness, porosity, and conductivity. Since graphite is highly conductive, adding more carbon blacks has little impact on its conductivity. Therefore, the conductivity of the anode is fixed. However, the conductivity of the cathode is highly dependent on the conductive additives and can be changed significantly during fabrication.

The battery cycle life optimization is to minimize the capacity degradation after long-term cycling while satisfying the energy density and power density requirements, which can be expressed by

$$\text{minimize } f_{degra}(x) = \frac{C(x)_1 - C(x)_{100}}{C(x)_1} \quad [29]$$

$$\text{subject to } \begin{cases} x_{lower} \le x \le x_{upper} \\ g_1(x) = P_{req} - P_{cell} \le 0 \\ g_2(x) = E_{req} - E_{cell} \le 0 \end{cases} \quad [30]$$

where P_{req} is the power density requirement and E_{req} is the energy density requirement.

To achieve a global optimum, multiple optimizations are performed starting with different initial values of the parameters as shown in Table II. This helps to avoid being trapped in local minima. For different sets of initial values, each parameter is varied within its reasonable range to achieve randomness. Note that the N/P ratio, which is the ratio of the negative electrode capacity (anode capacity) and positive electrode capacity (cathode capacity), is not an independent variable.

Table II. Four different sets of initial values used to start the optimization.

Parameters	1st set	2nd set	3rd set	4th set
Cathode particle radius (μm)	4	3	3.5	3
Cathode thickness (μm)	80	60	90	50
Cathode porosity	0.35	0.45	0.4	0.35
Cathode conductivity (S m^{-1})	3	2	1	1
Anode particle radius (μm)	6	7	5	12
Anode thickness (μm)	52	47	66	55
Anode porosity	0.3	0.47	0.3	0.55
N/P ratio	1.0133	1.1124	1.3109	0.9028

Table III summarizes the battery model parameters. The meanings of the parameters can be found in Ref. 12.

Table IV lists the key parameters for the side reactions. More details on the parameters can be found in Ref. 12. The damage function data for $LiMn_2O_4$ is not available yet in the literature. For demonstration purpose, here we assume a simple stress-based model,[20] $d\varepsilon_{usable}^{pos}(x,t)/dt = -k_{iso}|\sigma_h(x, r_p)|$, where k_{iso} is a coefficient taking different values for charge and discharge. This linear relation can be viewed as a first-order approximation. The stress on the particle surface is positive or tensile during lithium intercalation (discharge) and negative or compressive during lithium deintercalation (charge). k_{iso} is much smaller for charge than for discharge since the compressive strength of $LiMn_2O_4$ is much higher than its tensile strength.[15] Here the values of k_{iso} are determined by trial and error to fit the capacity degradation from simulation to experimental data.[12]

Table V lists the material parameters used to calculate the cell mass with Eq. 26. These material parameters are constants. The mass of the current collector or separator is calculated using density multiplied by volume. Calculating the mass of the electrode will use porosity, i.e. using $\varepsilon_1\rho_1 + \varepsilon_2\rho_2 + \varepsilon_3\rho_3$ multiplied by volume.

Results and Discussion

The power density requirement varies with applications. In this study it is chosen to be 2200 W kg^{-1}, which is in the range of reported values.[33,34] Due to the high complexity of the degradation model, each derivative evaluation takes about half an hour to compute.

Fig. 3 shows the evolution of power density, energy density, and design parameters with optimization iteration. The optimization algorithm maximizes the energy density for each set of initial parameters and adjusts the parameters to meet the power requirement. The power densities from the four set of different starting values all reach the power density requirement of 2200 W kg^{-1} after optimization. The energy densities increase to nearly 100 Wh kg^{-1} after optimization.

The optimized values for each set of initial values are listed in Table VI, which were obtained after 15 days of continuous calculation. The optimized parameters from different initial starting points have shown convergence. The averages of these values are used as the starting values for the subsequent battery cycle life optimization.

The energy density reaches about 100 Wh kg^{-1}, which is the maximum achievable density under the power requirement and material parameters used. To give the optimization algorithm some freedom to adjust the design parameters, we prescribe the required energy density a little smaller than the maximum achievable energy density. In this study we set the required energy density to be 86% of the maximum, or 86 Wh kg^{-1}. The values in the 'average' column of Table VI are used as the starting values for the battery cycle life optimization. The energy and power density requirements are used as constraints.

Table III. Cell level model parameters.

Parameter	Negative electrode	Separator	Positive electrode
Electrode thickness (m)	vary	20×10^{-6}	vary
Particle radius r_p (m)	vary		vary
Electrode porosity (electrolyte phase volume fraction) ε_2	vary	1	vary
Polymer and conductive filler volume fraction ε_3	0.172		0.259
Active material volume fraction ε_1	$1\text{-}\varepsilon_2\text{-}\varepsilon_3$		$1\text{-}\varepsilon_2\text{-}\varepsilon_3$
Solid phase conductivity k_1 (S m^{-1})	100		3.8
Effective conductivity of solid phase k_1^{eff} (S m^{-1})	$k_1^{eff} = k_1(\varepsilon_1)^p$		$k_1^{eff} = k_1(\varepsilon_1)^p$
Maximum solid phase concentration $c_{1,max}$ (mol m^{-3})	26390		22860
Solid phase Li diffusion coefficient D_1 (m^2 s^{-1})	3.9×10^{-14}		1×10^{-13}
Initial electrolyte concentration (mol m^{-3})	2000	2000	2000
Li transference number t_+^0	0.363	0.363	0.363
Electrolyte phase ionic conductivity k_2 (S m^{-1})		$k_2(c_2)$ curve	
Effective electrolyte phase ionic conductivity k_2^{eff} (S m^{-1})		$k_2^{eff} = k_2(\varepsilon_2)^p$	
Electrolyte phase Li diffusion coefficient D_2 (m^2 s^{-1})	7.5×10^{-11}	7.5×10^{-11}	7.5×10^{-11}
Effective electrolyte phase Li diffusion coefficient D_2^{eff} (m^2 s^{-1})		$D_2^{eff} = D_2(\varepsilon_2)^p$	
Electrolyte activity coefficient $f_{\pm}^+$	1	1	1
Bruggeman porosity exponent p	1.5	1.5	1.5
Charge transfers coefficient α_a, α_c	0.5		0.5
Reaction rate coefficient k_0 (m s^{-1})	2×10^{-11}		2×10^{-11}
Exchange current density i_0 (A m^{-2})		$Fk_0{c_2}^{\alpha_a}(c_{1,max} - c_{1,s})^{\alpha_a}{c_{1,\,s}}^{\alpha_c}$	
Active surface area per unit electrode volume a_s (m^{-1})	$3\varepsilon_1/r_p$		$3\varepsilon_{usable}^{pos}/r_p$
Faraday constant F (C mol^{-1})		96485.3415	
Initial electrode SOC (fresh cell)	0.01		0.99
Negative electrode equilibrium potential U_(V)	U_$(c_{1,s}/c_{1,max})$ curve		
Positive electrode equilibrium potential U$_+$(V)			U$_+(c_{1,s}/c_{1,max})$) curve
Partial molar volume of lithium ion Ω (m^3 mol^{-1})			3.5×10^{-6}
Poisson's Ratio v			0.3
Young's modulus E (GPa)			10

Table IV. Side reaction parameters.

Parameter	Value	Parameter	Value
k_{SEI}	4×10^{-10} m s^{-1}	α_a^{sol}	0.5
c_{EC}	4541 mol m^{-3}	U_{oxid}^{eq}	4.1 V
λ_{SEI}	1.2×10^7 m^{-1}	f_{H^+}	15%
α_c^{SEI}	0.5	X_c	10%
M_{SEI}	0.162 kg mol^{-1}	X_c^{ref}	10%
ρ_{SEI}	1690 kg m^{-3}	$a_c^{ref} i_0^{sol}$	3 A m^{-3}
k_{Mn_dep}	8×10^{-8} m s^{-1}	k_{decom}	7.13×10^{-10} m^6 mol^{-2} s^{-1}
$\alpha_c^{Mn\_dep}$	0.5	$D_{H^+}^{eff}$	$1 \times 10^{-10}{\varepsilon_2}^p$ m^2 s^{-1}
λ_{Mn_dep}	3×10^6 m^{-1}	$D_{Mn^{2+}}^{eff}$	$5 \times 10^{-11}{\varepsilon_2}^p$ m^2 s^{-1}
k_{H_2}	2.07×10^{-8} m s^{-1}	$D_{H_2O}^{eff}$	$3 \times 10^{-11}\ {\varepsilon_2}^p$ m^2 s^{-1}
λ_{H_2}	2×10^5 m^{-1}	$\bar{V}$	1.4×10^{-4} m^3 mol^{-1}
$\alpha_c^{H_2}$	0.5	k_{res}	3×10^4 Ω m
k_{dis}	2×10^{-9} m s^{-1}	$k_{iso,\ charge}$	2.5×10^{-15} Pa^{-1} s^{-1}
f_{Mn_dis}	40%	$k_{iso,\ discharge}$	8×10^{-13} Pa^{-1} s^{-1}

Fig. 4 shows the optimization process. The capacity fade after 100 cycles is decreased from 60% to 20% after optimization, rendering 200% improvement of battery cycle life, after a sacrifice of only 14% energy density. It should be noted that here the degradation is relative to the capacity of a fresh cell. A commercial battery cell will go through the formation cycle, during which the cell degrades relatively fast and ends up with a nominal capacity smaller than the fresh cell. Using the nominal capacity as a reference, the battery degradation will appear less both due to the smaller nominal capacity and the slowing down of degradation after the first few cycles. Therefore, the apparent improvement of battery cycle life after optimization will be less when using the nominal capacity as a reference.

The design parameters all converge to their optimal values as shown by the flat curves toward the end of iteration.

The optimized design parameters for battery cycle life are listed in Table VII. A comparison of the parameters before and after optimization shows that the most significant changes are the particle sizes of the anode and cathode.

Fig. 5 compares the cell performance before and after optimization during charge and discharge cycling. The capacity degradation is faster at the beginning and gradually slows down. After cycle life optimization, the capacity is very stable with cycling.

In order to better understand the degradation pattern between a normal cell and the optimized cell, we analyze the state of charge (SOC) swing windows of the cathode and of the anode separately during charge and discharge cycling. As shown in Fig. 6, the anode and cathode swing windows are quite stable with cycling after optimization. The degradation of the cell before cycle life optimization shows quickly shrinking SOC swing windows for both the anode and the cathode, which is mainly related to the reduction of cyclable lithium

Table V. Cell mass parameters.

Parameter	Negative electrode	Separator	Positive electrode
Active material density ρ_1 (Kg m^{-3})	2.15×10^3		4.1×10^3
Electrolyte density ρ_2 (Kg m^{-3})	1.16×10^3	1.16×10^3	1.16×10^3
Polymer and conductive filler density ρ_3 (Kg m^{-3})	1.78×10^3		1.78×10^3
Current collector density (Kg m^{-3})	8.96×10^3 (Cu)		2.7×10^3 (Al)
Current collector thickness (m)	15×10^{-6}		15×10^{-6}

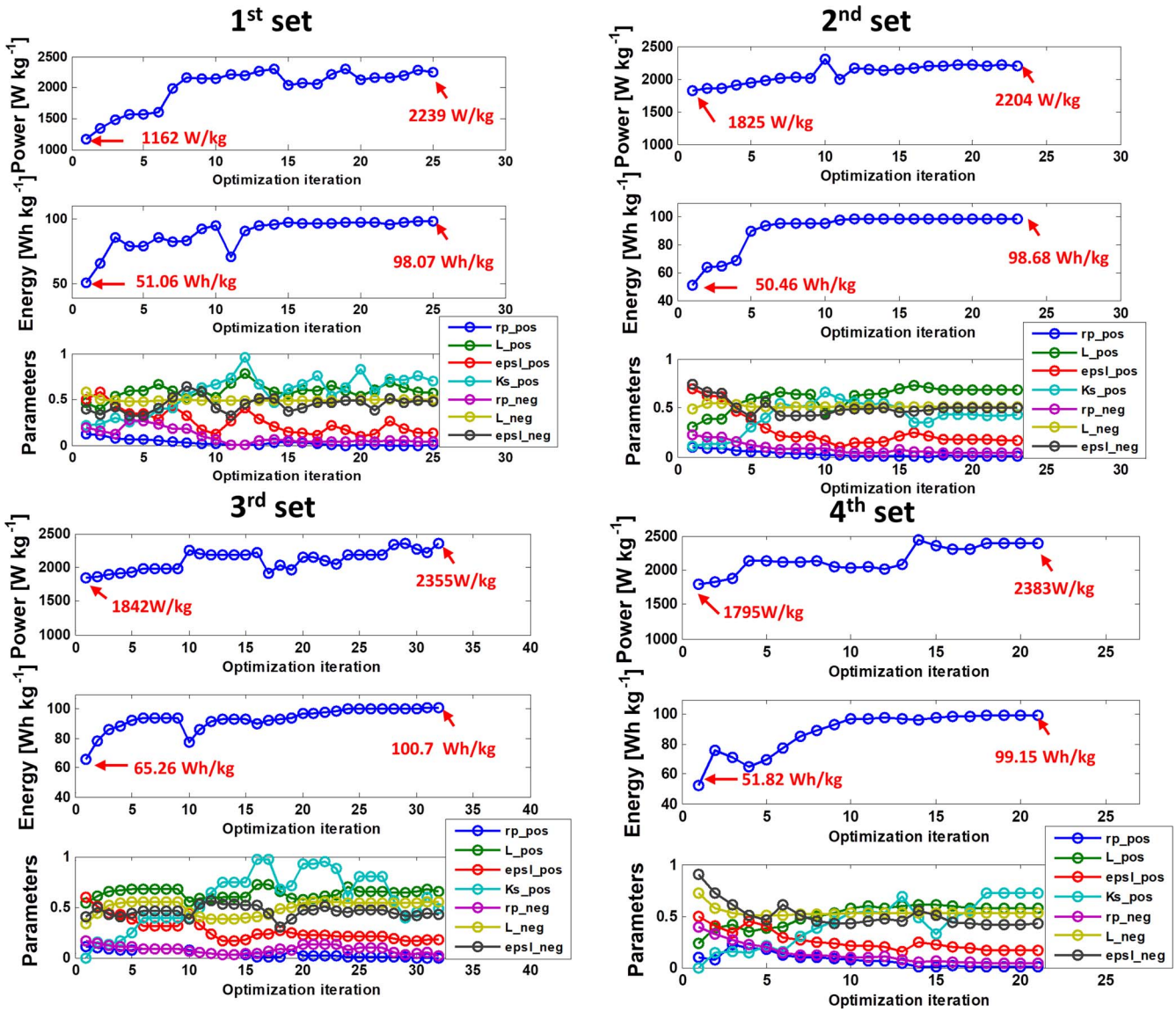

Figure 3. Energy density optimization with given power density requirement. The four sets show the evolution of power density, energy density, and design parameters with optimization iteration starting from different initial parameter values.

in the cell caused by the anode SEI growth. Before cycle life optimization, the anode particle size is small while the anode electrode thickness is large as a result of energy density optimization. These two together contribute to maximizing the energy density and satisfying the power density requirement. A large electrode thickness is resulted because in this way the active material accounts for a higher proportion of the total mass, which includes the mass of current collectors and the separator, as can be seen in Eq. 26. This effect plays an important role in increasing the energy density. For a thick anode, smaller particle size is required to meet the constraint of power density requirement. In other words, the resulting smaller particle size after energy optimization is mostly to match the thick electrode. Smaller particle size results in a larger total surface area of the particles, which leads to more SEI formation and smaller energy density. However, such negative effect on energy density from a small particle size is less significant in comparison to the benefit from a large electrode thickness,

Table VI. Optimized parameter values for maximizing the energy density while satisfying the power density requirement.

Parameters	Symbol	1st set	2nd set	3rd set	4th set	average
Cathode particle radius	rp_pos (μm)	0.45	0.51	0.21	0.38	0.39
Cathode thickness	L_pos (μm)	94.26	109.36	103.35	94.39	100.34
Cathode porosity	Epsl_pos	0.17	0.19	0.19	0.18	0.18
Cathode conductivity	Ks_pos (S m^{-1})	7.28	4.85	6.02	7.53	6.42
Anode particle radius	rp_neg (μm)	1.57	1.39	1.74	1.31	1.50
Anode thickness	L_neg (μm)	106.31	119.74	101.86	94.25	105.26
Anode porosity	epsl_neg	0.34	0.35	0.32	0.31	0.33
N/P ratio		1.1007	1.0787	1.0567	1.0787	1.0787

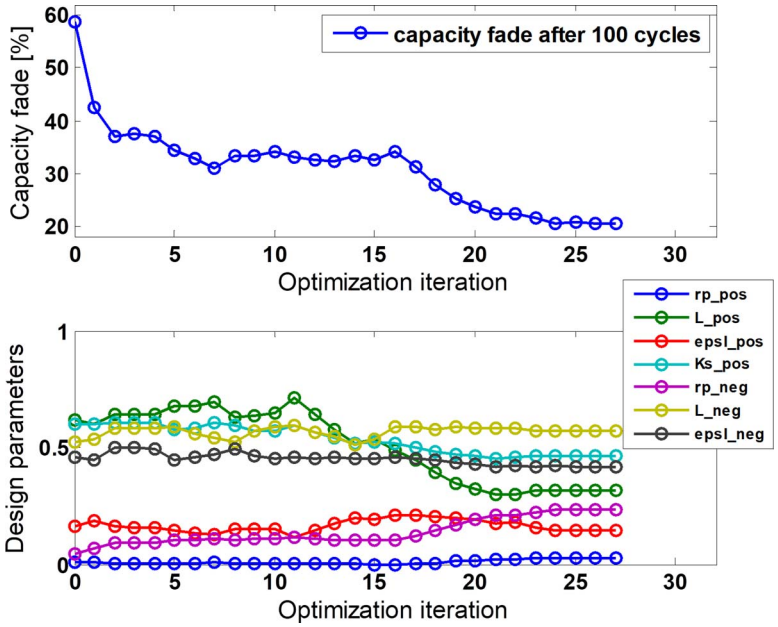

Figure 4. Battery cycle life optimization.

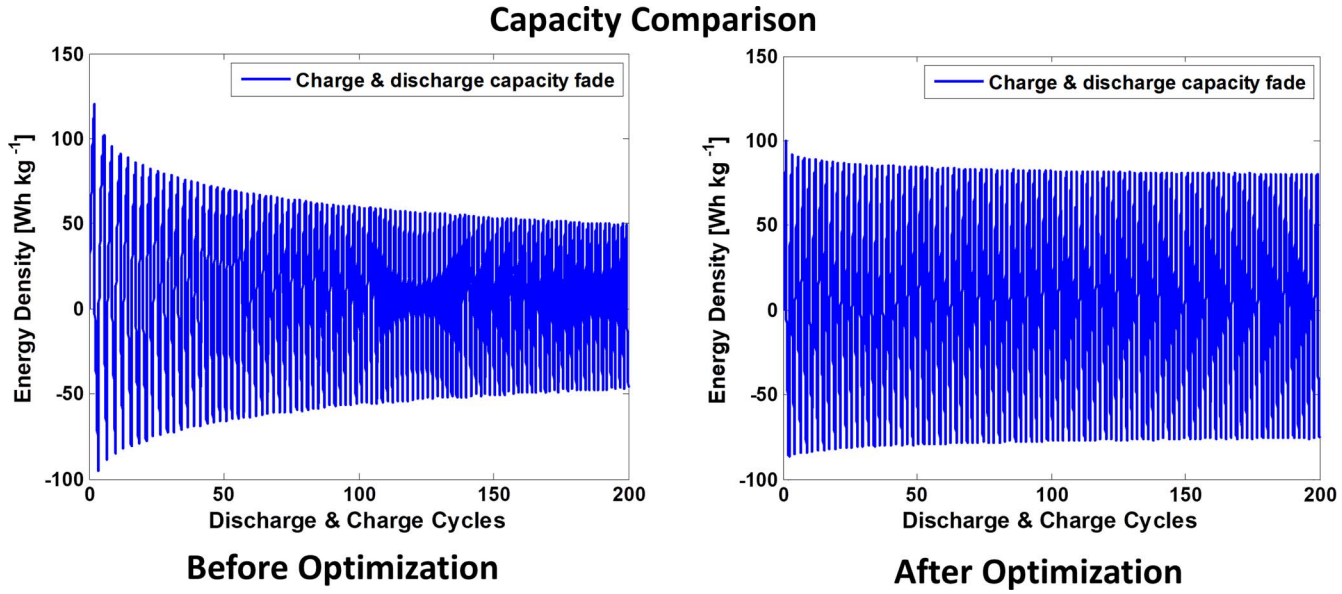

Figure 5. Comparison of capacity degradation between a normal cell and the optimized cell.

Table VII. Optimized parameter values for battery cycle life.

Parameters	Symbol	average	optimized for cycle life
Cathode particle radius	rp_pos (μm)	0.39	0.95
Cathode thickness	L_pos (μm)	100.34	61.12
Cathode porosity	Epsl_pos	0.18	0.17
Cathode conductivity	Ks_pos (S m^{-1})	6.42	5.18
Anode particle radius	rp_neg (μm)	1.50	7.08
Anode thickness	L_neg (μm)	105.26	60.00
Anode porosity	epsl_neg	0.33	0.31
N/P ratio		1.0787	1.0347
Degradation		60%	20%

since energy density involves very limited SEI formation in the first cycle only. Overall, energy optimization with the constraint of power density requirement prefers a thick electrode and a small particle size to match the thick electrode. After cycle life optimization, the anode particle size is increased to reduce SEI growth. Correspondingly, the anode electrode thickness is reduced to compensate for the power density loss owing to a larger particle size, so that the power density requirement is still satisfied. In cycle life optimization, the effect of particle size dominates because the SEI growth is accumulated over 100 cycles and the total effect is significant. In addition, because the energy density requirement is less than the maximum energy density, there is room to reduce the electrode thickness. Thus, cycle life optimization leads to a larger anode particle size. As a result, the SEI growth is suppressed and the SEI-induced cyclable lithium loss is reduced. The optimized cell shows a more balanced degradation from both the anode and the cathode, and a much improved overall cycle life.

We find that cyclable lithium loss is the dominating degradation mechanism during the first 200 cycles. Other mechanisms, such as stress-induced structural damage, play larger roles in much later cycles after the lithium loss stabilizes. A comparison of the cyclable lithium loss on the anode before and after optimization is shown in Fig. 7. The

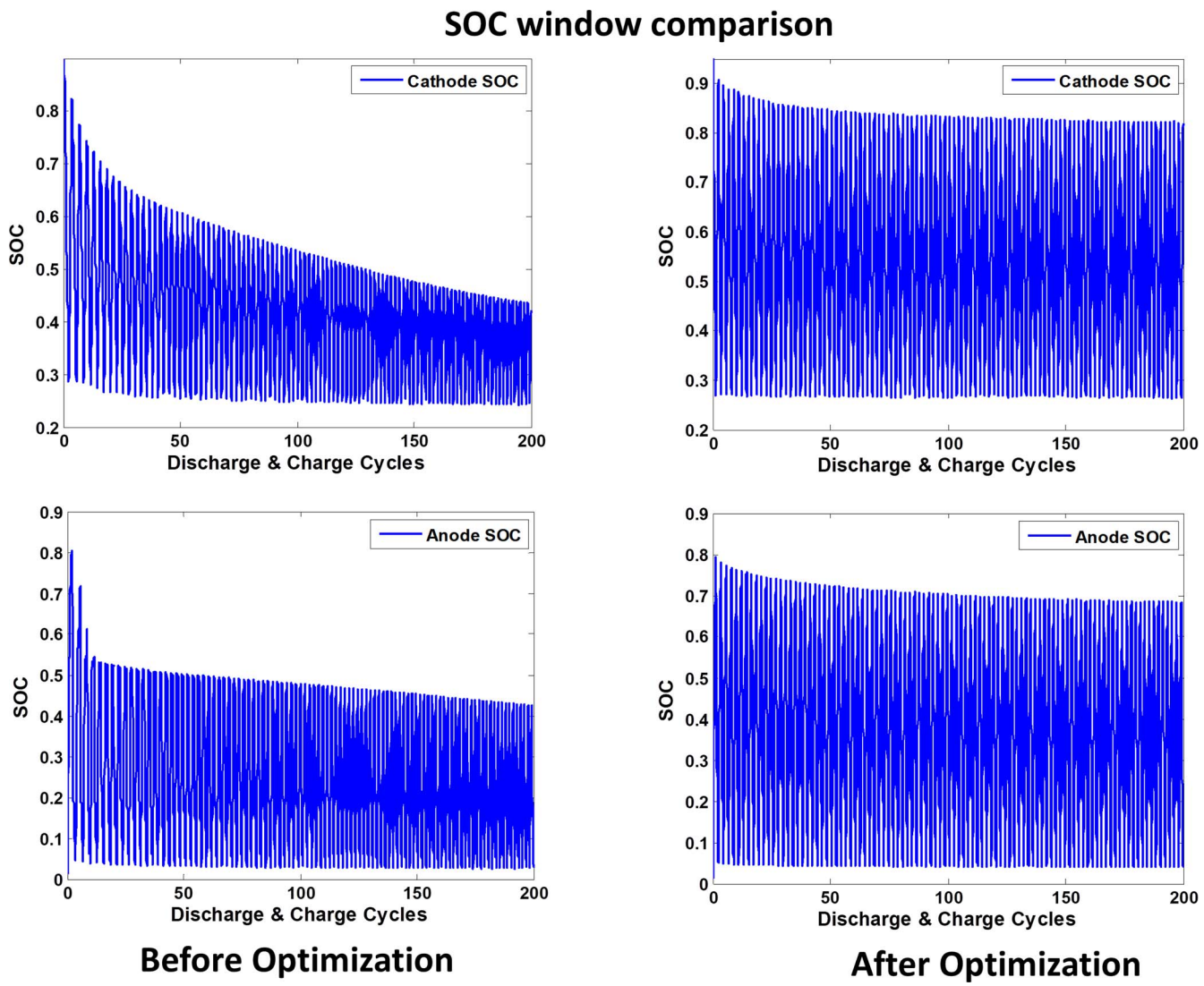

Figure 6. Comparison of the SOC swing window between a normal cell and the optimized cell.

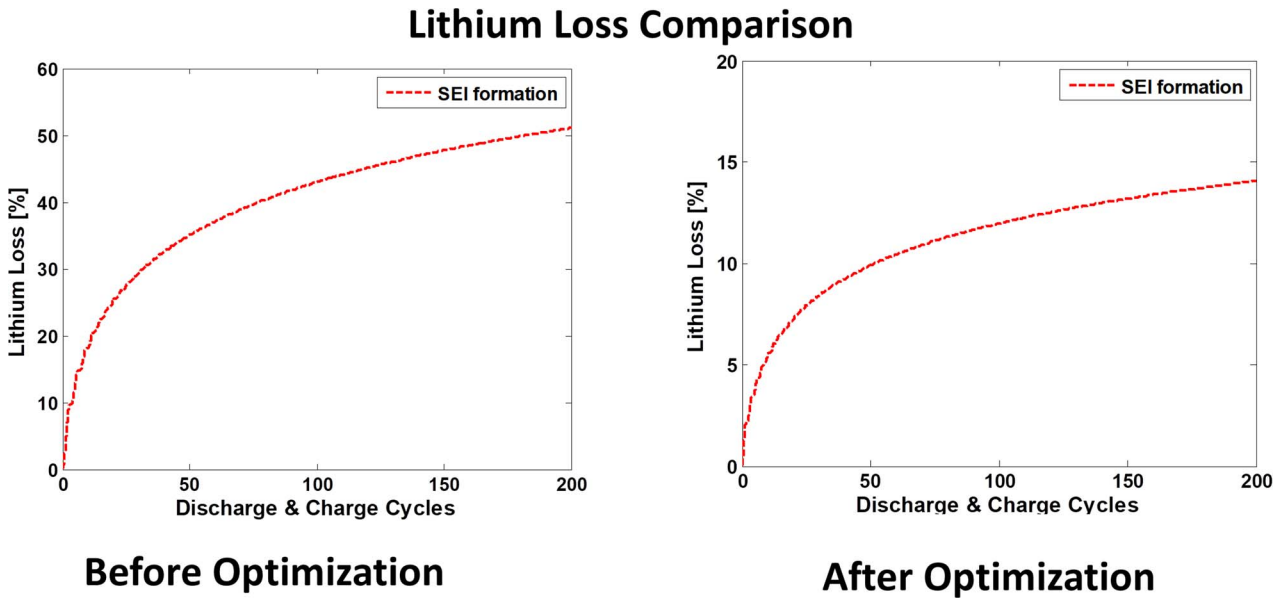

Figure 7. Cyclable lithium loss associated with SEI growth.

cell before cycle life optimization shows about 50% cyclable lithium loss after 200 cycles, while the optimized cell shows only 14% of cyclable lithium loss.

Conclusions

In this work we develop a general procedure to optimize battery cycle life while fulfilling the energy and power requirements. A gradient-based optimization algorithm is first applied for energy density optimization while satisfying the power density requirement. This maximum energy density serves as a reference to set an appropriate energy density requirement. Then the battery cycle life optimization is performed using the same optimization algorithm, which achieves significant cycle life improvement while satisfying the energy density and power density requirements. We find that energy density and power density optimization does not necessarily correlate to good battery cycle life. Higher energy and power densities require smaller particle sizes at both the anode and cathode, while better battery cycle life prefers larger particle size at the anode and smaller particle size at the cathode. The cyclable lithium loss is significantly reduced after battery cycle life optimization. While demonstrated with a specific battery chemistry system, the optimization procedure is broadly applicable. The results learned from this analysis can provide qualitative suggestions for improving battery cycle life in other systems. Our study highlights that energy density, power density, and battery cycle life should be considered together during optimization. The model and optimization approach developed in this study would be useful for battery design and manufacturing as well as the battery management strategy.

Acknowledgments

This work was supported by the National Science Foundation under grant No. CNS-1446117, and also partially supported by the Advanced Battery Coalition for Drivetrains at the University of Michigan. Support from our sponsor is gratefully acknowledged.

ORCID

Xianke Lin https://orcid.org/0000-0001-5695-248X
Wei Lu https://orcid.org/0000-0002-4851-1032

References

1. A. A. Pesaran, T. Markel, H. S. Tataria, and D. Howell, *Battery Requirements for Plug-in Hybrid Electric Vehicles-Analysis and Rationale*, National Renewable Energy Laboratory (2009).
2. B. Y. Liaw and M. Dubarry, *Journal of power sources*, **174**, 76 (2007).
3. S. G. Wirasingha, N. Schofield, and A. Emadi, in *IEEE Vehicle Power and Propulsion Conference*, p. 1 (2008).
4. R. Rao and S. Vrudhula, in *IEEE/ACM International Conference on Computer-Aided Design*, p. 439 (2005).
5. T. F. Fuller, M. Doyle, and J. Newman, *Journal of the Electrochemical Society*, **141**, 1 (1994).
6. D. Sumitava, P. W. Northrop, V. Ramadesigan, and V. R. Subramanian, *Journal of Power Sources*, **227**, 161 (2013).
7. S. J. Moura, J. L. Stein, and H. K. Fathy, *IEEE Trans. Control Sys. Tech.*, **21**, 679 (2012).
8. S. Moura, J. Forman, S. Bashash, J. Stein, and H. Fathy, *Industrial Electronics, IEEE Transactions on*, **58**, 3555 (2011).
9. P. Ramadass, B. Haran, R. White, and B. N. Popov, *Journal of Power Sources*, **123**, 230 (2003).
10. M. Safari, M. Morcrette, A. Teyssot, and C. Delacourt, *Journal of The Electrochemical Society*, **156**, A145 (2009).
11. Q. Zhang and R. E. White, *Journal of Power Sources*, **179**, 793 (2008).
12. X. Lin, J. Park, L. Liu, Y. Lee, A. Sastry, and W. Lu, *Journal of The Electrochemical Society*, **160**, A1701 (2013).
13. K. Smith and C.-Y. Wang, *Journal of Power Sources*, **161**, 628 (2006).
14. J. Newman, *Journal of the Electrochemical Society*, **142**, 97 (1995).
15. J. Christensen and J. Newman, *Journal of The Electrochemical Society*, **153**, A1019 (2006).
16. G. Amatucci, C. Schmutz, A. Blyr, C. Sigala, A. Gozdz, D. Larcher, and J. Tarascon, *Journal of Power Sources*, **69**, 11 (1997).
17. W. I. F. David, M. M. Thackeray, L. A. De Picciotto, and J. B. Goodenough, *Journal of Solid State Chemistry*, **67**, 316 (1987).
18. X. Zhang, W. Shyy, and A. M. Sastry, *Journal of the Electrochemical Society*, **154**, A910 (2007).
19. F. Yang, *Materials Science and Engineering: A*, **409**, 153 (2005).
20. S. Murakami, *Continuum Damage Mechanics: A Continuum Mechanics Approach to the Analysis of Damage and Fracture*, Springer, New York (2012).
21. V. Ramadesigan, R. N. Methekar, F. Latinwo, R. D. Braatz, and V. R. Subramanian, *Journal of The Electrochemical Society*, **157**, A1328 (2010).
22. V. Srinivasan and J. Newman, *Journal of the Electrochemical Society*, **151**, A1530 (2004).
23. J. Christensen, V. Srinivasan, and J. Newman, *Journal of The Electrochemical Society*, **153**, A560 (2006).
24. S. Stewart, P. Albertus, V. Srinivasan, I. Plitz, N. Pereira, G. Amatucci, and J. Newman, *Journal of The Electrochemical Society*, **155**, A253 (2008).
25. N. Xue, W. Du, T. A. Greszler, W. Shyy, and J. R. Martins, *Applied Energy*, **115**, 591 (2014).
26. J. C. Forman, S. J. Moura, J. L. Stein, and H. K. Fathy, *Journal of Power Sources*, **210**, 263 (2012).
27. K. C. Kiwiel, *Mathematical Programming*, **90**, 1 (2001).
28. S. P. Boyd and L. Vandenberghe, *Convex optimization*, Cambridge university press (2004).
29. P. Boggs and J. Tolle, *Acta Numerica*, **4**, 1 (1995).
30. S.-P. Han, *Journal of Optimization Theory and Applications*, **22**, 297 (1977).
31. M. J. Powell, in *Numerical analysis*, p. 144, Springer (1978).
32. P. E. Gill and E. Wong, in *Mixed integer nonlinear programming*, p. 147, Springer (2012).
33. T. Horiba, K. Hironaka, T. Matsumura, T. Kai, M. Koseki, and Y. Muranaka, *Journal of Power Sources*, **97**, 719 (2001).
34. W. F. Howard and R. M. Spotnitz, *Journal of Power Sources*, **165**, 887 (2007).